Chemical Science

ROYAL SOCIETY OF CHEMISTRY

EDGE ARTICLE

View Article Online
View Journal | View Issue

Open Access Article. Published on 18 November 2024. Downloaded on 1/23/2026 12:19:31 AM.
This article is licensed under a Creative Commons Attribution-NonCommercial 3.0 Unported Licence.

Check for updates

Cite this: *Chem. Sci.*, 2025, **16**, 378

All publication charges for this article have been paid for by the Royal Society of Chemistry

Received 8th October 2024
Accepted 16th November 2024

DOI: 10.1039/d4sc06818a

rsc.li/chemical-science

Enhanced electrocatalytic nitrate-to-ammonia performance from Mott–Schottky design to induce electron redistribution†

Ruikai Qi,‡[a] Qiuling Jiang,‡[bd] Li Deng,[a] Xianqiang Yu,[a] Bingyan Shi,[a] Mengxiao Zhong,*[c] Ying Wang*[b] and Xiaofeng Lu *[a]

Constructing highly efficient electrocatalysts *via* interface manipulation and structural design to facilitate rapid electron transfer in electrocatalytic nitrate-to-ammonia conversion is crucial to attaining superior NH_3 yield rates. Here, a Mott–Schottky type electrocatalyst of Co/In_2O_3 with a continuous fiber structure has been designed to boost the electrocatalytic nitrate-to-ammonia performance. The optimized Co/In_2O_3-1 catalyst exhibits an impressive NH_3 yield rate of 70.1 mg cm^{-2} h^{-1} at −0.8 V *vs.* the reversible hydrogen electrode (RHE), along with an NH_3 faradaic efficiency (FE) of 93.34% at 0 V *vs.* RHE, greatly outperforming the single-component Co and In_2O_3 samples. The yield rate of Co/In_2O_3-1 is also superior to that of most currently reported Co-based catalysts and heterostructured ones. Evidence from experiments and theoretical results confirms the formation of a Mott–Schottky heterojunction, which achieves a Co site enriched with electrons, coupled with an In_2O_3 facet enriched with holes, inducing an electron redistribution to promote the utilization of electroactive sites. Consequently, the reaction energy barrier for nitrate-to-ammonia conversion is significantly reduced, further enhancing its yield efficiency.

1. Introduction

NH_3 serves a variety of purposes, including fertilization, chemical production, and fuel.[1] In recent years, scientific research on electrocatalytic nitrate-to-ammonia conversion has gained extensive interest due to its advantages of safety, energy conservation, and eco-friendliness for NH_3 production.[2–10] However, the electrocatalytic nitrate-to-ammonia process involves complex multiple electron transfer and pathways, posing a great challenge to rational design and fabrication of efficient catalysts for electrochemical NH_3 generation.[11–19] Fortunately, some cost-effective transition metal-based materials hold promise as nitrate-to-ammonia electrocatalysts, particularly cobalt-based catalysts such as FeCoNiAlTi,[20] $Co_2Mo_6S_8$ (ref. 21) and $Ru_{15}Co_{85}$ (ref. 22) due to their superior intrinsic activities. Despite significant improvement in NH_3 faradaic efficiency (FE) that has been achieved at lower potentials, the NH_3 yield rates of those electrocatalysts are still unsatisfactory because of the low current density. Therefore, researchers relentlessly strive for exploring efficient nitrate reduction catalysts with high NH_3 yield.

Heterojunction structures significantly optimize the electronic structure and energy bands at catalyst interfaces, essential for rapid electron transfer. Consequently, at heterojunction interfaces, the adsorption of reactants, desorption of products, and the activity of active sites are promoted.[23–25] Typically, according to the Mott–Schottky effect, electrons in metal/semiconductor heterojunctions tend to spontaneously traverse interfaces until the work functions on both sides balance. This continuous adjustment at the interfaces alters the work function of the Mott–Schottky barrier, regulates the electron cloud density of the catalyst, and induces negative charge accumulation on the side with a higher work function.[26,27] Hence, creating Mott–Schottky junctions is a reliable strategy for modulating electron density at electrocatalyst interfaces. The construction of metal/semiconductor heterostructures with Mott–Schottky rectification effects holds potential for boosting the efficiency of the nitrate-to-ammonia reaction.

Indium oxide (In_2O_3) is a common n-type semiconductor with a wide bandgap, low resistivity, and high catalytic activity,

---

[a] Alan G. MacDiarmid Institute, College of Chemistry, Jilin University, Changchun 130012, P. R. China. E-mail: xflu@jlu.edu.cn

[b] State Key Laboratory of Rare Earth Resource Utilization, Changchun Institute of Applied Chemistry, Chinese Academy of Sciences, Changchun, 130022, China. E-mail: ywang_2012@ciac.ac.cn

[c] State Key Laboratory of Integrated Optoelectronics, Key Laboratory of Advanced Gas Sensors, College of Electronic Science and Engineering, Jilin University, 2699 Qianjin Street, Changchun, Jilin Province, 130012, P. R. China. E-mail: zhongmx@jlu.edu.cn

[d] School of Applied Chemistry and Engineering, University of Science and Technology of China, Hefei, 230026, China

† Electronic supplementary information (ESI) available. See DOI: https://doi.org/10.1039/d4sc06818a

‡ These authors contributed equally to this work.

© 2025 The Author(s). Published by the Royal Society of Chemistry

Open Access Article. Published on 18 November 2024. Downloaded on 1/23/2026 12:19:31 AM. This article is licensed under a Creative Commons Attribution-NonCommercial 3.0 Unported Licence.

which is widely used in electrocatalysis.[28–30] Therefore, we have demonstrated the clever construction of a continuous fibrous Mott–Schottky type Co/In_2O_3 heterostructure by combining Co with In_2O_3 through a simple electrospinning-calcination-partial reduction strategy. The experimental results demonstrate that the long-range ordered fiber network presents numerous active sites, and the formation of a Co/In_2O_3-1 heterojunction with the Mott–Schottky effect induces an electron redistribution at the interface, benefitting to reduce the reaction barrier of the catalytic process. Density functional theory (DFT) analysis indicates an augmentation of the density of states (DOS) near the Fermi level for the Co/In_2O_3-1 catalyst, and the d-band center (ε_d) of Co in Co/In_2O_3-1 aligns nearer to the Fermi level compared to Co (111). Therefore, Co/In_2O_3-1 exhibits the smallest thermodynamic reaction energy barrier (ΔG(PDS)) for the potential-determining step with the formation of NH_2^* from NH* protonation, suggesting that the Mott–Schottky type Co/In_2O_3 heterostructure significantly enhances the electrocatalytic nitrate-to-ammonia activity. Therefore, the optimized Co/In_2O_3-1 catalyst presents a high NH_3 yield rate of 70.1 mg cm^{-2} h^{-1} at −0.8 V *vs.* RHE, outperforming most currently reported nitrate-to-ammonia electrocatalysts.

2. Results and discussion

2.1 Synthesis and characterization of the Mott–Schottky type Co/In_2O_3 heterostructure

The nanofibrous Co/In_2O_3 heterostructure is synthesized using an electrospinning, calcination, and partial reduction process (Fig. 1a). Initially, a poly(vinylpyrrolidone) (PVP)/Co^{2+}/In^{3+} precursor nanofibrous membrane is prepared *via* an electrospinning technique and then immediately calcined in air to yield continuous and uniform Co_3O_4/In_2O_3 nanofibers with a rough surface and an average diameter of 144 nm (Fig. 1b and c). After being reduced in a H_2/Ar atmosphere at 400 °C for 4 h, Co_3O_4 can be selectively reduced, and then Co/In_2O_3 is obtained, and its fibrous morphology remains basically unchanged (Fig. 1d). However, the diameter of the Co/In_2O_3 nanofibers slightly decreases due to oxygen elimination (Fig. 1e). The transmission electron microscopy (TEM) image shows that Co/In_2O_3 nanofibers are composed of particles stacked together and have obviously porous characteristic (Fig. 1f). The high-resolution TEM (HRTEM) image (Fig. 1g) reveals 0.197 and 0.411 nm periodicities, corresponding to the (111) plane of Co and (211) plane of In_2O_3, respectively, and discernible grain boundaries can be observed, demonstrating the successful formation of the Co/In_2O_3 heterostructure. Fig. 1h exhibits the selected area electron diffraction (SAED) pattern, presenting legible rings attributed to the crystal planes of Co and In_2O_3, suggesting a polycrystalline characteristic of Co and In_2O_3. Moreover, the energy dispersive X-ray (EDX) spectrum presents strong Co, In and O signals in Co/In_2O_3-1 (Fig. S1, ESI†). Elemental mapping displays homogeneous distribution of these elements throughout the Co/In_2O_3-1 nanofiber (Fig. 1i). In addition, a series of control catalysts with diverse contents of Co are prepared using the same synthesis method, named In_2O_3-H, Co/In_2O_3-0.5, and Co/In_2O_3-2 (Fig. S2 and S3, ESI†), which exhibit similar nanofibrous morphologies and average diameters. And the inductively coupled plasma-optical emission spectrometry (ICP-OES) results confirm that

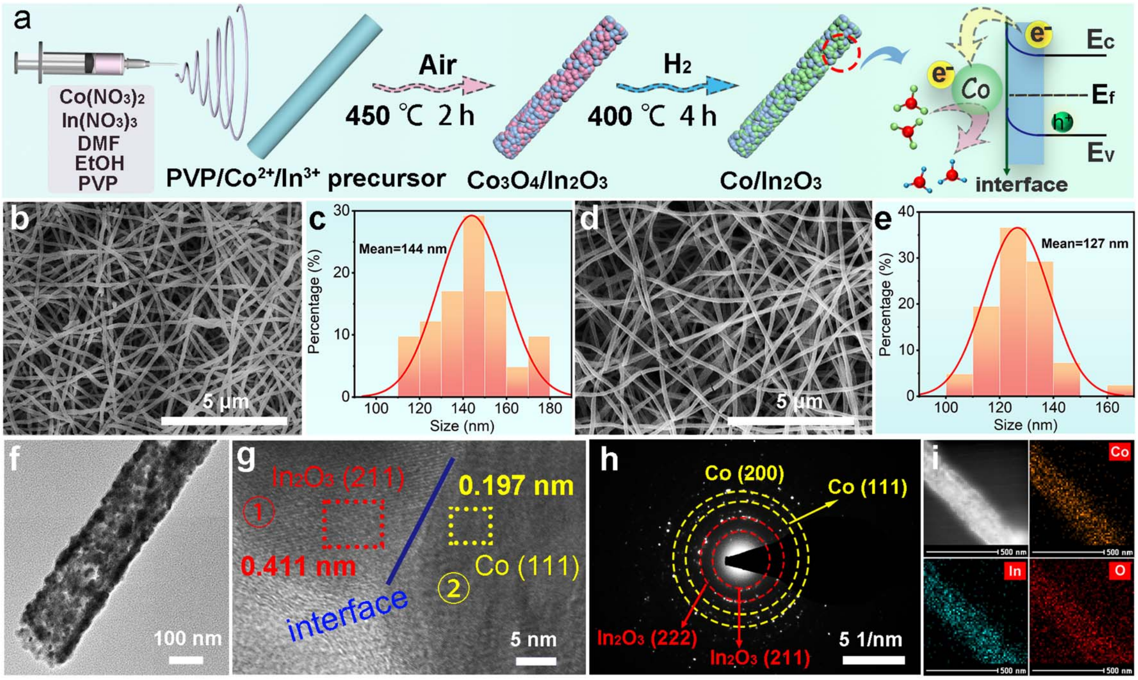

Fig. 1 (a) Synthesis procedure of Co/In_2O_3. (b) SEM image and (c) diameter distribution of Co_3O_4/In_2O_3 nanofibers. (d) SEM image and (e) diameter distribution of Co/In_2O_3 nanofibers. (f) TEM, (g) HRTEM and (h) SAED images of Co/In_2O_3. (i) HAADF-STEM image and EDX element mappings of Co–K, In–L, and O–K.

© 2025 The Author(s). Published by the Royal Society of Chemistry

Open Access Article. Published on 18 November 2024. Downloaded on 1/23/2026 12:19:31 AM.
This article is licensed under a Creative Commons Attribution-NonCommercial 3.0 Unported Licence.

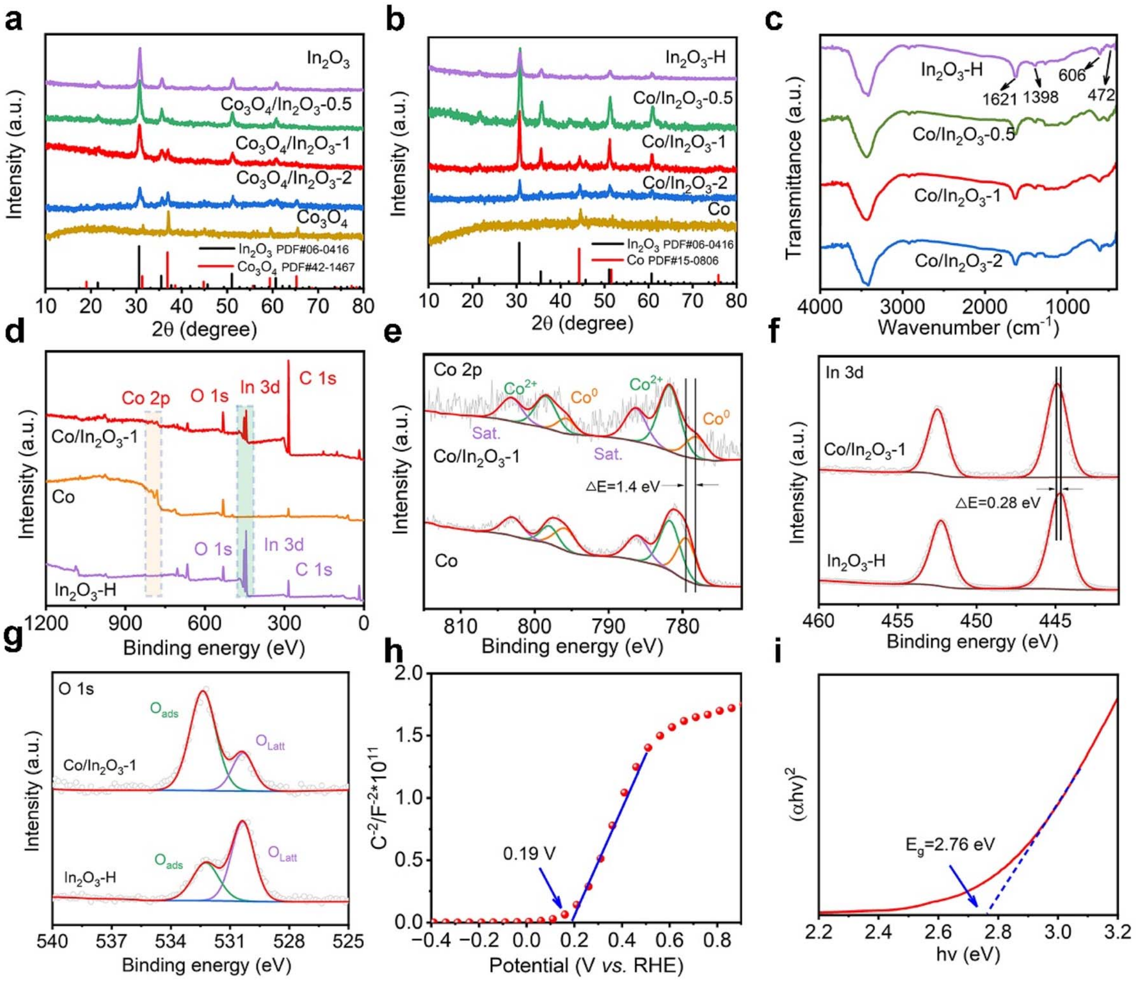

Fig. 2 (a) XRD profiles of In_2O_3, Co_3O_4/In_2O_3-0.5, Co_3O_4/In_2O_3-1, Co_3O_4/In_2O_3-2 and Co_3O_4. (b) XRD profiles of In_2O_3–H, Co/In_2O_3-0.5, Co/In_2O_3-1, Co/In_2O_3-2 and Co. (c) FTIR spectra of In_2O_3-H, Co/In_2O_3-0.5, Co/In_2O_3-1 and Co/In_2O_3-2. (d) XPS survey spectra of Co/In_2O_3-1, Co, and In_2O_3–H. Typical narrow-scan (e) Co 2p, (f) In 3d and (g) O 1s XPS spectra of different catalysts. (h) Mott–Schottky plot and (i) Tauc plot of In_2O_3-H.

the molar ratio and feeding amount of Co and In are almost the same (Table S1, ESI†). After bare Co_3O_4 is reduced to Co metal, the fiber morphology collapses, reflecting that the presence of In_2O_3 can maintain the stability of the structure (Fig. S4, ESI†).

X-ray diffraction (XRD) analysis identifies the obtained Co_3O_4/In_2O_3 products (Fig. 2a), exhibiting both In_2O_3 (PDF #06-0416) and Co_3O_4 (PDF #42-1467) phases. After H_2/Ar reduction treatment at 400 °C, XRD analysis exhibits the disappearance of Co_3O_4 peaks, replaced by those of Co (PDF #15-0806), while In_2O_3 is still in the oxide phase, demonstrating the formation of the Co/In_2O_3 heterostructure (Fig. 2b). Here, the effect of the H_2/Ar reduction temperature on Co/In_2O_3 synthesis is investigated. From Fig. S5 (ESI),† it can be seen that when the temperature is below 400 °C, Co_3O_4 cannot be completely reduced, while a high temperature can destroy the In_2O_3 crystal structure. Therefore, the temperature of 400 °C is chosen as the optimal experimental condition. Fig. 2c displays the Fourier transform infrared (FTIR) spectra of In_2O_3-H, Co/In_2O_3-0.5, Co/In_2O_3-1, and Co/In_2O_3-2 samples. The peaks at 472 and 606 cm^{-1} of all the as-prepared Co/In_2O_3 samples correspond to the In–O bond vibration, while those at 1398 and 1621 cm^{-1} are related to adsorbed water molecules. Due to the metallic properties of Co, the characteristic peaks of Co/In_2O_3 composites are completely consistent with those of In_2O_3-H.[31]

The X-ray photoelectron spectroscopy (XPS) test further assesses valence states of the components in the Co/In_2O_3-1 sample. Fig. 2d shows that Co/In_2O_3-1 nanofibers discern the presence of Co, In and O elements. The narrow scan Co 2p XPS spectrum yields six distinct peaks (Fig. 2e),[32,33] notably at 778.1 eV and 795.7 for Co nanoparticles, aligning with the XRD results. The spin–orbit peaks at 781.8 and 798.6 eV correspond to Co $2p_{3/2}$ and Co $2p_{1/2}$, respectively, and the peaks at 786.3 and 803.2 eV are satellite peaks. In the In 3d core-level spectrum, In $3d_{5/2}$ and In $3d_{3/2}$ spin orbit peaks appear at 444.9 and 452.5 eV (Fig. 2f).[34,35] Notably, the Co $2p_{3/2}$ binding energy (BE) of Co/In_2O_3-1 presents a negative shift of 1.4 eV relative to Co, while In $2p_{5/2}$ undergoes a positive shift of 0.28 eV compared with In_2O_3-H, signifying electron transfer from In_2O_3 to Co in the

Open Access Article. Published on 18 November 2024. Downloaded on 1/23/2026 12:19:31 AM.
This article is licensed under a Creative Commons Attribution-NonCommercial 3.0 Unported Licence.

heterostructure. Fig. 2g presents the O 1s XPS spectra of Co/In_2O_3-1 and In_2O_3-H, identifying two dominant peaks at a BE of 530.4 and 532.2 eV, indicating the lattice (O_{Latt}) and the surface adsorbed oxygen (O_{ads}), respectively. The ratio of $O_{ads}/(O_{ads} + O_{latt})$ in Co/In_2O_3-1 is higher than that in In_2O_3-H, suggesting more surface oxygen defects accessible in Co/In_2O_3-1.[36]

Rationally engineered Mott–Schottky interfaces stimulate spontaneous electron transfer, substantially enhancing charge transfer efficiency. The Mott–Schottky data for In_2O_3-H material are depicted in Fig. 2h, where the positive slope and the *x*-intercept suggest n-type In_2O_3-H possessing a flat band potential of 0.19 V (*vs.* RHE). The Tauc plot (Fig. 2i) derived from the UV-vis result (Fig. S6a, ESI†) indicates a bandgap of 2.76 eV. It is generally accepted that the flat band potential of n-type semiconductors is usually employed to approximate the conduction band, typically lying between 0.1 and 0.3 eV below the Fermi level. Therefore, the band relationship suggests that the heterojunction formed by Co and In_2O_3 conforms to the Mott–Schottky model (Fig. S6b, ESI†).

2.2 Evaluation of electrocatalytic nitrate-to-ammonia performances

The electrocatalytic nitrate-to-ammonia performance is evaluated in 1.0 M KOH with 0.1 M KNO_3. Initially, a substantial augmentation of current density occurs in the presence of KNO_3, demonstrating that the electrocatalytic nitrate-to-ammonia reaction possesses higher activity than the hydrogen evolution reaction (HER). The current density and onset potential of the obtained Co/In_2O_3 is also larger than that of individual Co, In_2O_3-H, and Co_3O_4/In_2O_3, demonstrating that the catalyst with the Mott–Schottky heterostructure exhibits a higher catalytic activity (Fig. S7, ESI†). Furthermore, the effect of the feeding ratio of Co to the In precursor on the electrocatalytic activity has also been revealed. By comparing the LSV curves of varied catalysts with 80% *iR*-compensation, it is preliminarily believed that Co/In_2O_3-1 has the highest ammonia production activity due to its largest current density (Fig. 3a). Afterwards, using electrochemical impedance spectroscopy

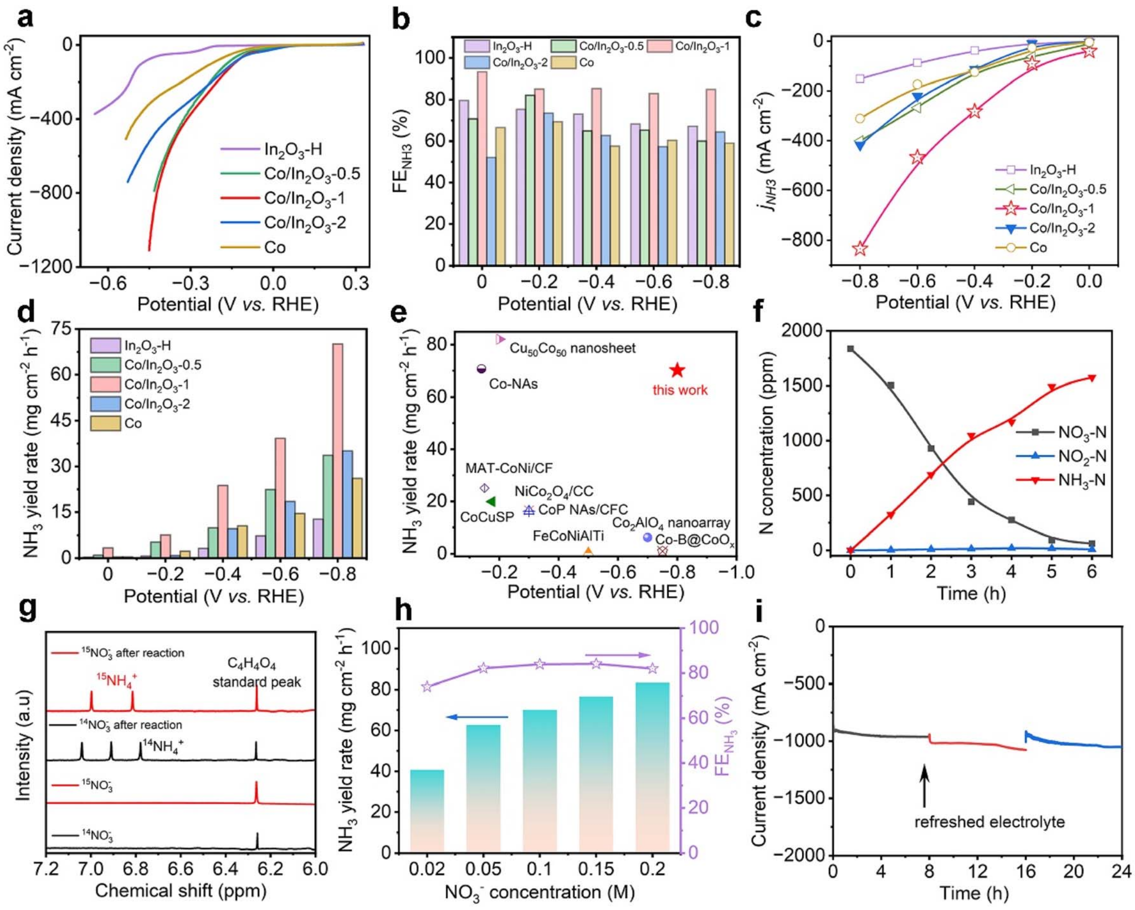

Fig. 3 (a) LSV curves of In_2O_3–H, Co/In_2O_3-0.5, Co/In_2O_3-1, Co/In_2O_3-2 and Co with 80% *iR*-correction. (b) NH_3 FE, (b) j_{NH_3} and (d) NH_3 yield rate of In_2O_3-H, Co/In_2O_3-0.5, Co/In_2O_3-1, Co/In_2O_3-2 and Co at varied potentials. (e) Comparison of the NH_3 yield rate of Co/In_2O_3-1 at a potential of −0.8 V for 1 h of electrocatalytic nitrate-to-ammonia conversion with that of other reported catalysts. (f) Time-dependent concentration changes of NO_3–N, NO_2–N and NH_3–N during the electrocatalytic nitrate-to-ammonia reaction by Co/In_2O_3-1 at −0.8 V in 1 M KOH with an initial concentration of 1800 mg L^{-1} of NO_3–N. (g) NMR spectra of the products produced before and after the electrocatalytic nitrate-to-ammonia reaction by Co/In_2O_3-1 in the electrolyte of 1 M KOH with 0.1 M $K^{15}NO_3$ and 0.1 M $K^{14}NO_3$ at −0.8 V. (h) The NH_3 FEs and NH_3 yield rate of Co/In_2O_3-1 at −0.8 V in the electrolyte of 1 M KOH with varied concentrations of KNO_3. (i) Chronoamperometric curves of Co/In_2O_3-1 at −0.8 V in 3 cycles, and each cycle lasting for 8 h of long-term electrolysis.

Open Access Article. Published on 18 November 2024. Downloaded on 1/23/2026 12:19:31 AM. This article is licensed under a Creative Commons Attribution-NonCommercial 3.0 Unported Licence.

(EIS), we evaluate the charge-transfer kinetics (Fig. S8, ESI†). After calculation and fitting, the charge transfer resistance of Co/In_2O_3-1 is calculated to be 6.89 Ω, which is lower than that of other control samples including In_2O_3-H (246 Ω), Co (14.14 Ω), Co/In_2O_3-0.5 (57.67 Ω), and Co/In_2O_3-2 (9.61 Ω). This signifies faster charge transfer and optimal electrocatalytic kinetics of Co/In_2O_3-1, benefitting the enhanced nitrate-to-ammonia performance. Cyclic voltammetry (CV) is executed, with the double-layer capacitance (C_{dl}) determined through potential scanning in the non-faraday region (Fig. S9, ESI†). The C_{dl} of Co/In_2O_3-1 is 3.2 mF cm^{-2}, larger than those of In_2O_3-H (1.7 mF cm^{-2}), Co/In_2O_3-0.5 (3.1 mF cm^{-2}), Co/In_2O_3-2 (1.8 mF cm^{-2}) and Co (2.0 mF cm^{-2}), showcasing more active sites to boost the nitrate-to-ammonia efficiency (Fig. S10, ESI†).

Chronoamperometry and UV-vis examinations are performed to determine the NH_3 yield rate and FE (Fig. S11–S14, ESI†). Initially, the NH_3 FE exceeds that of NO_2^- across diverse catalyst electrodes at different electrolysis voltages, indicating domination of NH_3 as the electrolysis product (Fig. S15, ESI†). As depicted in Fig. 3b, the NH_3 FE of Co/In_2O_3-1 reaches 93.34% at 0 V, surpassing that of In_2O_3-H (79.67% at 0 V), Co/In_2O_3-0.5 (82.16% at −0.2 V), Co/In_2O_3-2 (73.53% at −0.2 V) and Co (69.41% at −0.2 V). Concurrently, Co/In_2O_3-1 exhibits higher NH_3 partial current densities (j_{NH_3}) across various potentials, suggesting its superior electrocatalytic nitrate-to-ammonia activity over the entire potential range (Fig. 3c). Fig. 3d reveals an augmentation in the NH_3 yield rate with a decrease in applied potential for the as-synthesized catalysts. Notably, the NH_3 yield rate of Co/In_2O_3-1 outperforms that of In_2O_3-H, Co/In_2O_3-0.5, Co/In_2O_3-2 and Co over the entire potential range, thanks to its exceptional NH_3 FE and j_{NH_3}. Specifically, at a potential of −0.8 V, the NH_3 yield rate of Co/In_2O_3-1 reaches 70.1 mg cm^{-2} h^{-1}, superior to that of In_2O_3-H (12.7 mg cm^{-2} h^{-1}), Co/In_2O_3-0.5 (33.7 mg cm^{-2} h^{-1}), Co/In_2O_3-2 (35.1 mg cm^{-2} h^{-1}) and Co (26.1 mg cm^{-2} h^{-1}). Additionally, as depicted in Fig. 3e and Table S2 (ESI),† the NH_3 yield rate of Co/In_2O_3-1 also surpasses that of many Co-based and other heterostructured nitrate-to-ammonia catalysts reported so far, suggesting that this cost-effective and efficient Co/In_2O_3-1 has the potential for large-scale NH_3 production. To evaluate the efficiency of Co/In_2O_3-1 in nitrate removal, a batch experiment is conducted with an initial NO_3^-–N concentration of around 1800 ppm to detect the remaining products (Fig. 3f). Remarkably, nearly all NO_3^-–N sources are reduced within 6 h, with an impressive NH_3–N selectivity of 88.7%. Following 6 h of electrolysis, NO_3^- is almost removed and there is nearly no obvious NO_2^- formation. These findings demonstrate that Co/In_2O_3-1 achieves an outstanding activity and NH_3 FE, showing potential for nitrate removal/conversion in wastewater. Subsequently, isotope labeling experiments ascertain the source of NH_3 (Fig. 3g). Compared to the negligible peak of NH_4^+ before electrolysis, the ^1H NMR spectrum of the $^{14}NO_3^-$ solution reveals three different $^{14}NH_4^+$ peaks, while the $^{15}NO_3^-$ solution features a notable $^{15}NH_4^+$ double peak after 1 h of electrolysis at −0.8 V, demonstrating the origination of the produced ammonia from KNO_3 reduction.

Next, the concentration of KNO_3 in the electrolyte is adjusted to range from 0.02 M to 0.2 M to evaluate the environmental compatibility of Co/In_2O_3-1 for the electrocatalytic nitrate-to-ammonia reaction. First, as the KNO_3 concentration increases, the onset potential and current density increase as expected (Fig. S16, ESI†), accompanied by a progressive increase in the NH_3 yield rate, reaching 83.3 mg cm^{-2} h^{-1} at a KNO_3 concentration of 0.2 M (Fig. 3h). Second, the NH_3 FE consistently remains above 80%, indicating that Co/In_2O_3-1 maintains efficient electrocatalytic nitrate-to-ammonia activity across a broad concentration range. To assess the stability of Co/In_2O_3-1 during nitrate-to-ammonia electrocatalysis, we conducted three cycle tests with a total 24-h electrocatalysis at −0.8 V (Fig. 3i). The catalytic current density remains steady throughout the test. Moreover, the NH_3 FE and yield rate remain consistent in the different cycles, with average values of 69.24% and 58.3 mg cm^{-2} h^{-1}, affording evidence for the ideal durability of the Co/In_2O_3-1 catalyst for electrocatalytic nitrate-to-ammonia conversion (Fig S17, ESI†).

2.3 The investigations of the nitrate-to-ammonia reaction mechanism

Owing to the multiple reactive sites on the Co/In_2O_3-1 catalyst, the charge density difference is determined prior to investigating the nitrate-to-ammonia reaction mechanism. The red circle in the charge density difference in Fig. S18 (ESI)† highlights the Co/In_2O_3-1 interface with a relatively enhanced charge density, suggesting these locations as preferential adsorption sites for nitrate reduction. According to the previous study,[37] the possible reaction pathways of the nitrate reduction process are illustrated in Fig. 4a. Fig. S19–S21 (ESI)† illustrate the optimal structures of reaction intermediates on Co (111), In_2O_3 (211), and Co/In_2O_3-1, respectively, along the most conductive reaction pathway. The free energy diagrams for nitrate reduction are depicted in Fig. 4b, revealing varied favorable pathways for nitrate reduction on Co (111), In_2O_3 (211), and Co/In_2O_3-1, predominantly arising from the NOH* hydrogenation step. Upon protonating NOH* on the Co (111) surface, we observe its tendency towards forming N* and producing H_2O, with a reaction energy of −1.67 eV. However, on both In_2O_3 (211) and Co/In_2O_3-1, the formation of HNOH* is energetically favored after NOH* protonation. Notably, this process on In_2O_3 (211) is endothermic with an energy requirement of 2.28 eV, and it becomes spontaneous on Co/In_2O_3-1, exhibiting an exothermic reaction energy of −0.69 eV. The PDS analysis reveals the catalytic potential for nitrate-to-ammonia conversion on the three catalysts. On Co (111), the PDS is identified as the formation of HNO_2^*, with a corresponding reaction energy (ΔG(PDS)) of 0.66 eV. On In_2O_3 (211), NOH* hydrogenation is regarded as the PDS, exhibiting the highest ΔG(PDS) value of 2.28 eV. The high thermodynamic energy barriers on both Co (111) and In_2O_3 (211) suggest that these two catalysts are unlikely to facilitate nitrate-to-ammonia efficiently. However, on Co/In_2O_3-1, the protonation of NH* to form NH_2^* appears as the PDS, with a ΔG(PDS) of merely 0.15 eV. This remarkably small ΔG(PDS) signifies the significant synergistic enhancement of nitrate-to-ammonia catalytic activity of Co/In_2O_3-1 by the strong

© 2025 The Author(s). Published by the Royal Society of Chemistry

Open Access Article. Published on 18 November 2024. Downloaded on 1/23/2026 12:19:31 AM.
This article is licensed under a Creative Commons Attribution-NonCommercial 3.0 Unported Licence.

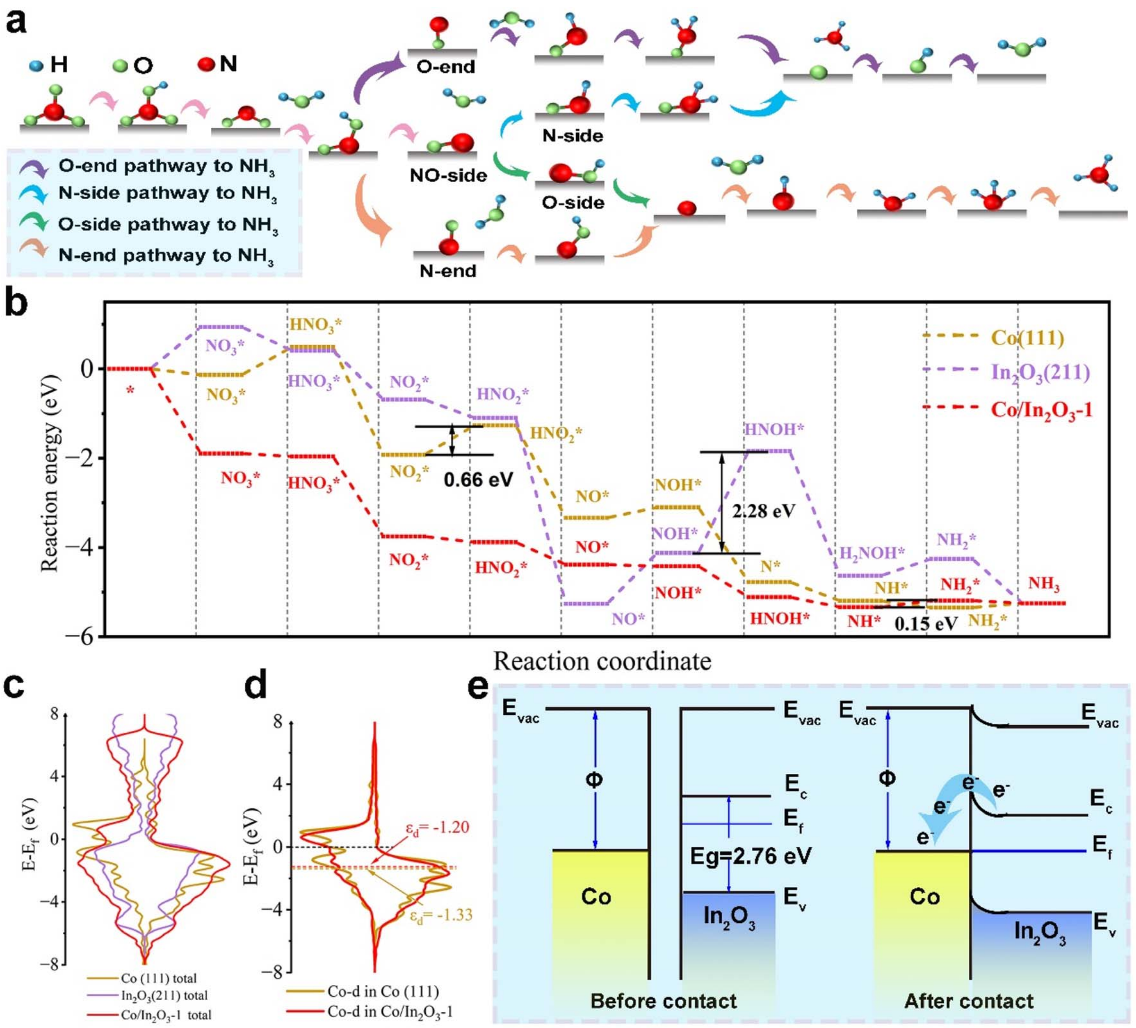

Fig. 4 (a) Illustration of potential reaction pathways of electrocatalytic nitrate-to-ammonia conversion. (b) Free energy diagrams for electrocatalytic nitrate-to-ammonia conversion on Co (111), In_2O_3 (211), and Co/In_2O_3. (c) Total density of states (TDOS) of Co (111), In_2O_3 (211), and Co/In_2O_3. (d) Projected density of states (PDOS) of the Co d orbital in the Co (111) and Co/In_2O_3. (e) The energy band diagrams of metallic Co and semiconductor In_2O_3 before and after the formation of a Mott–Schottky heterojunction.

interaction between Co and In_2O_3. This result is corroborated by studying the electronic attributes of these three catalysts. As shown in Fig. 4c, the density of states (DOS) near the Fermi level for Co/In_2O_3-1 noticeably increases compared to the In_2O_3 (211) substrate, suggesting improved electrical conductivity of Co/In_2O_3. Moreover, as shown in Fig. 4d, the d band center (ε_d) of Co in Co/In_2O_3-1 is −1.20 eV, situated 0.13 eV above the Fermi level compared to the value of Co in Co (111) (−1.33 eV). This shift not only strengthens the catalyst-intermediate interaction, but also further validates the beneficial impact of the Co–In_2O_3 interaction on the enhanced electrocatalytic activity of Co/In_2O_3-1.

Fig. 4e presents the energy band diagram of the Co/In_2O_3 heterojunction, illustrating the mechanism behind its promoted nitrate-to-ammonia performance. This enhancement is attributed to the prompt and spontaneous electron transfer from In_2O_3 to Co, facilitated by the elevated Fermi level of In_2O_3. Upon intimate contact, the In_2O_3 band drops, achieving equilibrium between Fermi levels of Co and In_2O_3. This forms a rectifying Schottky junction in the depletion region to generate a charge density gradient and result in an electron-rich zone at the Co side and a hole-rich region at the In_2O_3 side, creating a built-in electric field to provide a directed electron flow path. This electron reallocation is forecast to augment electroactive site utilization, lower reaction energy thresholds, and speed up the overall reaction kinetics. Therefore, the Co/In_2O_3-1 heterojunction electrocatalyst exhibits a superior NH_3 FE and high NH_3 yield rate during the nitrate-to-ammonia process.

2.4 Zn–NO_3^- battery

Finally, an aqueous Zn–NO_3^- battery is constructed with Co/In_2O_3-1 as the cathode and Zn foil as the anode (Fig. S22a, ESI†), achieving both energy production and NH_3 manufacturing. Due to the excellent electrocatalytic nitrate-to-ammonia performance of Co/In_2O_3-1, the Zn–NO_3^- battery exhibits a consistent open circuit voltage of 1.388 V *vs.* Zn within 1000 s (Fig. S22b,

Open Access Article. Published on 18 November 2024. Downloaded on 1/23/2026 12:19:31 AM.
This article is licensed under a Creative Commons Attribution-NonCommercial 3.0 Unported Licence.

ESI†). In addition, a peak power density of 2.15 mW cm^{-2} is achieved (Fig. S22c, ESI†). Fig. S23a (ESI)† illustrates the discharging curves of the Zn–NO_3^- battery at different current densities for 1 h, demonstrating stable battery voltage. An NH_3 yield rate of 1.36 mg h^{-1} cm^{-2} at 20 mA cm^2 is observed (Fig. S23b, ESI†). This suggests that the nitrate-to-ammonia process has outstanding application prospects in practical power generation devices, concurrently producing valuable NH_3 industrial products.

3. Conclusion

In summary, a Co/In_2O_3 heterostructure with the Mott–Schottky effect is ingeniously constructed through electrospinning, calcination, and partial reduction techniques. The experimental results reveal the spontaneous electron flow from In_2O_3 to Co at the interface, achieving an electron redistribution in the Co/In_2O_3 heterojunction to improve the utilization of active sites. Theoretical findings further prove that the ε_d of Co in Co/In_2O_3-1 is closer to the Fermi level than that of Co in Co (111), with Co/In_2O_3-1 exhibiting the smallest ΔG(PDS). This suggests that the remarkable synergistic interaction between Co and In_2O_3 significantly boosts the nitrate-to-ammonia catalytic activity of Co/In_2O_3-1. This work offers fresh perspectives for the thoughtful design of efficient Mott–Schottky heterojunction electrocatalysts for electrocatalytic nitrate-to-ammonia conversion.

Data availability

Data supporting the findings of this study are available within the article ESI.†

Author contributions

R. Qi and Q. Jiang contributed equally to this work. X. Lu, Y. Wang and M. Zhong conceived the experiments and supervised this project. R. Qi performed the experiments. R. Qi, L. Deng, X. Yu, and B. Shi characterized the catalysts and analyzed the data. Q. Jiang and Y. Wang carried out the theoretical calculation. R. Qi and Q. Jiang wrote the manuscript. All authors have approved the final version of the manuscript.

Conflicts of interest

The authors declare no conflict of interest.

Acknowledgements

This work was financially supported by the National Natural Science Foundation of China (52273056 and 22373097) and the Jilin Province Science and Technology Development Program (20220101056JC). Part of the computational time is supported by the High Performance and Computing Center of Jilin Province, Network and Computing Center in Changchun Institute of Applied Chemistry, Chinese Academy of Sciences, and Computing Center in Jilin Normal University.

References

1 J. Galloway, A. Townsend, J. Erisman, M. Bekunda, Z. Cai, J. Freney, L. Martinelli, S. Seitzinger and M. Sutton, *Science*, 2008, **320**, 889.

2 H. Xu, Y. Ma, J. Chen, W. Zhang and J. Yang, *Chem. Soc. Rev.*, 2022, **51**, 2710.

3 J. Liang, Z. Li, L. Zhang, X. He, Y. Luo, D. Zheng, Y. Wang, T. Li, H. Yan, B. Ying, S. Sun, Q. Liu, M. Hamdy, B. Tang and X. Sun, *Chem*, 2023, **9**, 1768.

4 Y. Xiong, Y. Wang, J. Zhou, F. Liu, F. Hao and Z. Fan, *Adv. Mater.*, 2023, **36**, 2304021.

5 H. Zhang, H. Wang, X. Cao, M. Chen, Y. Liu, Y. Zhou, M. Huang, L. Xia, Y. Wang, T. Li, D. Zheng, Y. Luo, S. Sun, X. Zhao and X. Sun, *Adv. Mater.*, 2024, **36**, 2312746.

6 L. Ouyang, J. Liang, Y. Luo, D. Zheng, S. Sun, Q. Liu, M. Hamdy, X. Sun and B. Ying, *Chin. J. Catal.*, 2023, **50**, 6.

7 T. Xie, X. He, L. He, K. Dong, Y. Yao, Z. Cai, X. Liu, X. Fan, T. Li, D. Zheng, S. Sun, L. Li, W. Chu, A. Farouk, M. Hamdy, C. Xu, Q. kong and X. Sun, *Chin. Chem. Lett.*, 2024, **35**, 110005.

8 J. Miao, Q. Hong, L. Liang, G. Li, Z. Liu, S. Yin and Y. Chen, *Chin. Chem. Lett.*, 2024, **35**, 108935.

9 C. Cang and H. Zheng, *Chin. J. Struct. Chem.*, 2023, **42**, 100143.

10 Y. Kim, J. Ko, M. Shim, J. Park, H. Shin, Z. Kim, Y. Jung and H. Byon, *Chem. Sci.*, 2024, **15**, 2578.

11 Q. Hong, B. Miao, T. Wang, F. Li and Y. Chen, *Energy Lab.*, 2023, **1**, 220022.

12 K. Dong, Y. Yao, H. Li, H. Li, S. Sun, X. He, Y. Wang, Y. Luo, D. Zheng, Q. Liu, Q. Liu, D. Ma, X. Sun and B. Tang, *Nat. Synth.*, 2024, **3**, 763.

13 Y. Wang, C. Wang, M. Li, Y. Yu and B. Zhang, *Chem. Soc. Rev.*, 2021, **50**, 6720.

14 J. Zhou, M. Wen, R. Huang, Q. Wu, Y. Luo, Y. Tian, G. Wei and Y. Fu, *Energy Environ. Sci.*, 2023, **16**, 2611.

15 Z. Y. Wu, M. Karamad, X. Yong, Q. Huang, D. A. Cullen, P. Zhu, C. Xia, Q. Xiao, M. Shakouri, F. Y. Chen, J. Kim, Y. Xia, K. Heck, Y. Hu, M. Wong, Q. Li, L. Gates, S. Siahrostami and H. Wang, *Nat. Commun.*, 2021, **12**, 2870.

16 F. Y. Chen, Z. Y. Wu, S. Gupta, D. J. Rivera, S. V. Lambeets, S. Pecaut, J. Y. T. Kim, P. Zhu, Y. Z. Finfrock, D. M. Meira, G. King, G. Gao, W. Xu, D. Cullen, H. Zhou, Y. Han, D. Perea, C. Muhich and H. Wang, *Nat. Nanotechnol.*, 2022, **17**, 759.

17 Y. Wang, M. Sun, J. Zhou, Y. Xiong, Q. Zhang, C. Ye, X. Wang, P. Lu, T. Feng, F. Hao, F. Liu, J. Wang, Y. Ma, J. Yin, S. Chu, L. Gu, B. Huang and Z. Fan, *Proc. Natl. Acad. Sci. U. S. A.*, 2023, **120**, e2306461120.

18 Z. Zhang, A. Niu, Y. Lv, H. Guo, J. S. Chen, Q. Liu, K. Dong, X. Sun and T. Li, *Angew. Chem., Int. Ed.*, 2024, **63**, e202406441.

19 J. Liang, P. Liu, Q. Li, T. Li, L. Yue, Y. Luo, Q. Liu, N. Li, B. Tang, A. A. Alshehri, I. Shakir, P. Agboola, C. Sun and X. Sun, *Angew. Chem., Int. Ed.*, 2022, **61**, e202202087.

© 2025 The Author(s). Published by the Royal Society of Chemistry

Open Access Article. Published on 18 November 2024. Downloaded on 1/23/2026 12:19:31 AM.
This article is licensed under a Creative Commons Attribution-NonCommercial 3.0 Unported Licence.

20 R. Zhang, Y. Zhang, B. Xiao, S. Zhang, Y. Wang, H. Cui, C. Li, Y. Hou, Y. Guo, T. Yang, J. Fan and C. Zhi, *Angew. Chem., Int. Ed.*, 2024, **63**, e202407589.

21 B. Li, F. Xia, Y. Liu, H. Tan, S. Gao, J. Kaelin, Y. Liu, K. Lu, T. J. Marks and Y. Cheng, *Nano Lett.*, 2023, **23**, 1459.

22 S. Han, H. Li, T. Li, F. Chen, R. Yang, Y. Yu and B. Zhang, *Nat. Catal.*, 2023, **6**, 402.

23 Z. Huang, J. Song, Y. Du, S. Xi, S. Dou, J. M. V. Nsanzimana, C. Wang, Z. J. Xu and X. Wang, *Nat. Energy*, 2019, **4**, 329.

24 R. Qi, L. Zhang, S. Ren, B. Shi, M. Zhong, Z. Chen and X. Lu, *Nano Lett.*, 2024, **24**, 8964.

25 Z. Sun, Y. Wang, L. Zhang, H. Wu, Y. Jin, Y. Li, Y. Shi, T. Zhu, H. Mao, J. Liu, C. Xiao and S. Ding, *Adv. Funct. Mater.*, 2020, **30**, 1910482.

26 X. Li, Y. Pan, H. Yi, J. Hu, D. Yang, F. Lv, W. Li, J. Zhou, X. Wu, A. Lei and L. Zhang, *ACS Catal.*, 2019, **9**, 4632.

27 Y. Li, W. Wang, B. Zhang, L. Fu, M. Wan, G. Li, Z. Cai, S. Tu, X. Duan, Z. W. Seh, J. Jiang and Y. Sun, *Nano Lett.*, 2021, **21**, 6656.

28 Y. Zhang, Z. Li, C. Qiang, K. Chen, Y. Guo and K. Chu, *ACS Nano*, 2024, **18**, 25316.

29 H. Sun, S. Lee, R. Tang, L. Wang, C. Yang, W. Liang, S. Zhao, C. Dong, A. Soon and J. Huang, *Adv. Funct. Mater.*, 2024, 2415859.

30 D. Deng, Y. Wang, J. Jiang, Y. Bai, Y. Chen, H. Zheng, H. Ou and Y. Lei, *Chem. Commun.*, 2024, **60**, 9364.

31 Q. Liang, S. Zhao, Z. Li, Z. Wu, H. Shi, H. Huang and Z. Kang, *ACS Appl. Mater. Interfaces*, 2021, **13**, 40754.

32 C. Liu, Y. Li, T. Peng, S. Luo, Y. Feng, W. Xie, D. Lu and W. Sun, *J. Power Sources*, 2020, **468**, 228393.

33 W. Li, S. Chen, M. Zhong, C. Wang and X. Lu, *Chem. Eng. J.*, 2021, **415**, 128879.

34 X. Zhou, J. Wu, Q. F. Li, T. Zeng, Z. Ji, P. He, W. G. Pan, X. M. Qi, C. Y. Wang and P. K. Liang, *J. Catal.*, 2017, **355**, 26.

35 Q. Wang, Y. J. Chen, X. Liu, L. G. Li, L. Z. Du and G. H. Tian, *Chem. Eng. J.*, 2021, **421**, 129968.

36 J. Ding, Z. Geng, L. Li, Y. Wang, Y. Zuo, H. Li, M. Yang and G. Li, *J. Mater. Chem. A*, 2021, **9**, 12623.

37 L. Lv, Y. Shen, J. Liu, X. Meng, X. Gao, M. Zhou, Y. Zhang, D. Gong, Y. Zheng and Z. Zhou, *J. Phys. Chem. Lett.*, 2021, **12**, 11143.

© 2025 The Author(s). Published by the Royal Society of Chemistry